# High Temperature Superconducting Energy Storage Techniques

Jian Xun Jin[1], Zheng Guang Wang[1], You Guang Guo[2] and Jian Guo Zhu[2]
[1]Center of Applied Superconductivity and Electrical Engineering,
University of Electronic Science and Technology of China, China
[2]Faculty of Engineering, University of Technology, Sydney, Australia

With the development of applicable high temperature superconducting (HTS) materials, energy storages made using the HTS materials become available for practical applications. The HTS energy storage operational principles, techniques and their applications are summarized and analyzed in this paper.

*Key Words:* High temperature superconductors, Energy storages, Coils, Flywheels.

## 1. Introduction

Superconducting energy storages typically include: (i) SMES, which stands for Superconducting Magnetic Energy Storage, and (ii) SFWES, which stands for Superconducting Flywheel Energy Storage.

A SMES stores energy in the magnetic field created by a DC current flowing through a superconducting coil and released when it is required. A typical SMES system includes a superconducting coil or magnet to store energy, an AC/DC converter to interface between the superconducting coil and the electric power network, a protection system for the superconducting coil and the AC/DC converter, a cooling system for the superconducting coil and an automatic controller to coordinate the system operation. In the recent 30 years, SMES technology is one of the very active research areas especially after the high temperature superconducting (HTS) materials were discovered in 1986.

A typical SFWES energy storage device mainly consists of HTS levitators and permanent magnets for friction-free bearing, and a reciprocal motor/generator component for electrical energy conversion. It is an integrated system of a kind of building block system.

HTS has been identified as a suitable technology to develop practical SMES and SFWES [1]-[11]. The HTS energy storage operational principles, techniques and their applications are summarized and analyzed in this paper.

**Correspondence:** Jian Xun Jin, Center of Applied Superconductivity and Electrical Engineering, University of Electronic Science and Technology of China, Chengdu 610054, China, email: jxjin@uestc.edu.cn.

## 2. SMES

A SMES system is normally consists of a superconducting coil with a cryogenic system and a protection system, a power conditioning system and a controller, as shown in Fig. 1 [12]. The superconducting coil obtains energy during charging from the power system, and releases the energy stored through discharging. The energy stored in the superconducting coil can be described as follow

$$E = LI^2 / 2 \tag{1}$$

where $L$ is the inductance of the SMES coil, $I$ is the current flowing in the SMES coil. If the SMES coil discharges with constant power $P_0$ within time $t_s$, the energy in the SMES coil $E(t)$ at $t<t_s$ is

$$E(t) = E_s - P_0 t \tag{2}$$

When $t = t_s$, $I = I_s$ and

$$I_s = \frac{P_0}{v} \tag{3}$$

where $v$ is the voltage across the coil during discharge.

If the current in the coil drops below $I_s$, the system can no longer discharge with constant power $P_0$. However discharge may be continued at a reduced power and this depends on the depth of discharge. The term depth of discharge $\lambda$ of the coil is represented as a ratio of deliverable energy $E_d$ to stored energy $E_S$

$$\lambda = \frac{E_d}{E_S} = \frac{P_0 t_s}{E_S} \tag{4}$$

The current at any given time $t$ is obtained from (1) and (3) as

$$I(t) = \frac{P_0}{v\sqrt{1-\lambda}}\sqrt{1-\lambda\frac{t}{t_s}} \tag{5}$$

This current depends on the depth of discharge and the coil operating voltage. The energy stored at any given time $t$ is obtained from (2) and (4) as

$$E(t) = E_S - \frac{E_S \lambda}{t_s} t = \frac{P_0 t_s}{\lambda}(1 - \lambda \frac{t}{t_s}) \quad (6)$$

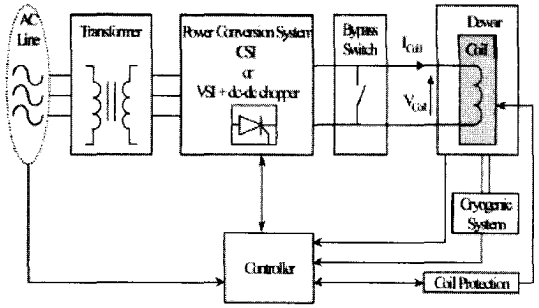


Fig. 1. Components of a typical SMES system

## 3. SFWES

In order to reduce the rotary frictional dissipation, magnetic suspension bearing systems are generally used, which can be divided into the passive magnetic suspension bearing (PMB) and the active magnetic suspension bearing (AMB).

Fig. 2 is the principle structure of HTS magnetic levitation SFWES having following features [13]: (i) The superconductor is cooled to the superconducting state, and with a permanent magnet PM to form magnetic suspension. The PM bears the weight of the energy storage flywheel. (ii) The electrical machinery runs by way of motor, and change the electric energy into the kinetic energy to store. Conversely, when the electrical machinery runs by way of dynamotor, the kinetic energy stored of flywheel will be changed into the electric energy. (iii) To reduce the energy lose on the rotary flywheel, the flywheel and magnetic suspension bearing are generally put in a vacuum environment. The vacuum environment is the adiabatic means keeping the low temperature of the superconductor.

Fig. 3 shows the operation principle of an energy storage system using the flywheel [14]. A flywheel energy storage system (FESS) has three work model (i) Charge - An AC electrical source supplies power for the flywheel controller, the flywheel controller controls the electric energy input to make the flywheel reach the highest working rotational speed. (ii) Maintaining energy - The flywheel system relies on the minimum alternating current to import energy and to keep the flywheel running in the highest working rotational speed. (iii) Discharge - When required by the AC power electric side, the flywheel supplies power, the controller offers incessant power to its load, the rotational speed of the flywheel drops.

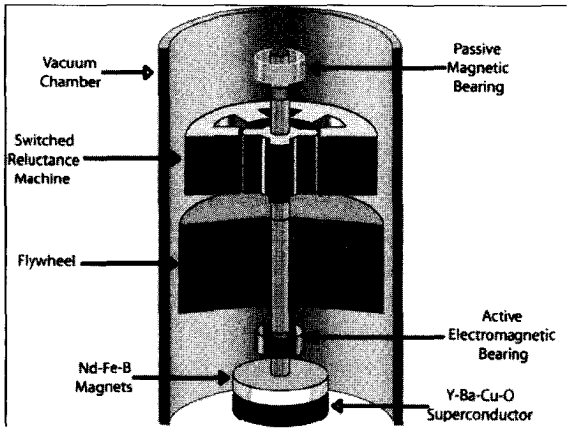


Fig. 2. Scheme of the proposed flywheel energy storage system

Calculation of HTS levitation force $F_{Lev}$ between a PM and a HTS based on Ampere's force $f$ is related to current density $J$ as

$$\vec{f} = \vec{J} \times \vec{B} \quad (7)$$

Levitation force is given by

$$\vec{F}_{Fev} = \iiint_{V_{SC}} \vec{f}\, dV = \iiint_{V_{SC}} dV\left(\vec{J}_{SC} \times \vec{B}\right) = \iiint_{V_{SC}} dV\left(\vec{J}_{SC} \times \vec{B}_{PM}\right) + \iiint dV\left(\vec{J}_{SC} \times \vec{B}_{SC}\right) \quad (8)$$

$$\because \iiint_{V_{SC}} dV\left(\vec{J}_{SC} \times \vec{B}_{SC}\right) = 0$$

$$\therefore \vec{F}_{Lev} = \iiint_{V_{SC}} dV(\vec{J}_{SC} \times \vec{B}_{PM}) \quad (9)$$

where $V$ is volume, $V_{SC}$ is HTS volume, $J_{SC}$ is supercurrent density distribution, $B$ is magnetic flux density, $B_{PM}$ is PM magnetic flux density, and $B_{SC}$ is for HTS.

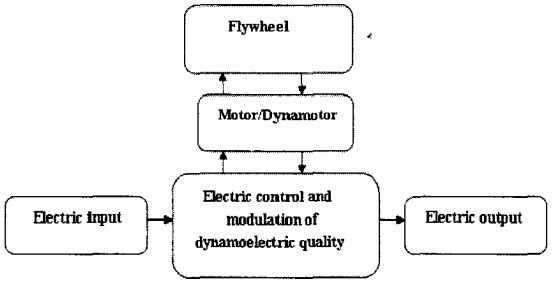


Fig. 3. Principle frame of a FESS

The basic HTS magnetic levitation SFWES mainly has following features. If the rotor quality is $m$, and with the linear speed of $v$, the kinetic energy $E$ is

$$E = \frac{1}{2}mv^2 \tag{10}$$

Rotary inertia $I$ is

$$I = \int_m r^2 dm \tag{11}$$

and

$$E = \frac{1}{2}I\omega^2 \tag{12}$$

where $\omega$ is angular speed, and $r$ is rotor radius. This is the energy that the flywheel is stored. In addition, the function of uneven moment $M$, stands for the quality of the flywheel rotor, is the main reason which the rotational speed of the flywheel changes, and the relation is

$$M = I\frac{d\omega}{dt} \tag{13}$$

When the rotary direction of torque of $M$ is same to the direction of flywheel, $M$ is turning forward, the flywheel is accelerated and stores the kinetic energy. When the rotary direction of torque of $M$ is opposite to the direction of flywheel, $M$ is reverse at this moment, the flywheel is decelerated, release the kinetic energy. The energy stored and released is

$$E = \frac{1}{2}I\left(\omega_{max}^2 - \omega_{min}^2\right) \tag{14}$$

If loss is neglected, its density of power is

$$P = \frac{dE}{dt} = \frac{d\left(I\omega^2\right)}{2\times dt} = M\omega \tag{15}$$

Energy stored per unit weight of the flywheel is

$$e = E/m = 9.8\times K_s \times \sigma_b/\rho \tag{16}$$

where $K_s$ stands for the flywheel shape coefficient, $\sigma_b$ stands for the permitted stress of the material, $\rho$ stands for the material density. Quality energy density is $e_m = E/m = K_s\left(\sigma_b/\rho\right)$; volume energy density is $e_V = E/V = K_s\sigma_b$ ; and performance - price ratio is $e_C = E/C = K_s\left(\sigma_b/C\rho\right)$, where $C$ stands for the unit quality price, $K_s$ stands for the flywheel shape coefficient ($K_s \leq 1$). According to the formula above, the flywheel material is better to have bigger $\sigma_b/\rho$. Usually $\sigma_b/\rho$ of carbon fibre materials is higher than other materials, and is generally selected at present. The energy density of present flywheel systems can reach 20 Wh/kg, the density of power can reach 5 kW/kg.

## 4. Control Technology

Power conditioning systems (PCS) are the interface from the SMES coil to power systems, generally there are two types: current source converter (CSC) PCS as shown in Fig. 4 and voltage source converter (VSC) PCS as shown in Fig. 5. The configurations of CSC-PCS and VSC-PCS have been introduced [15]. The control strategies of PCS are such as (i) Phase-shifting sinusoidal pulse width modulation SPWM technology, and (ii) Non-linear robust control and fuzzy control.

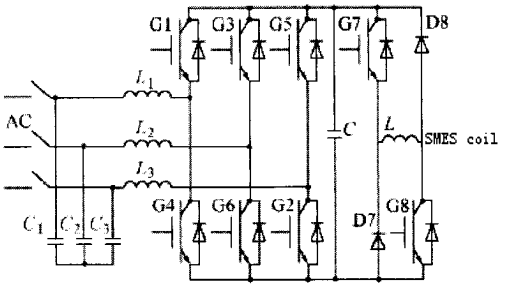


Fig. 4. Voltage source converter of PCS

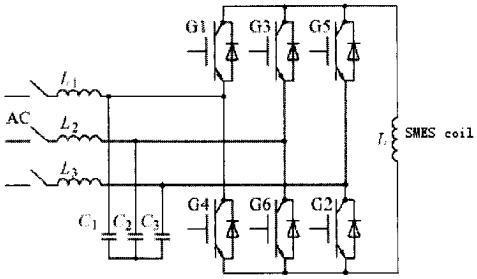


Fig. 5. Current source converter of PCS

The SFWES magnetic bearing control system can be made using a displacement sensor, controller, power amplifier and electric magnet as shown Fig. 6.

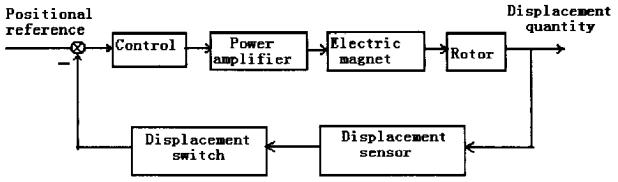


Fig. 6. The scheme of SFWES single channel control loop

## 5. Conclusion

HTS energy storage operational principles, techniques and their applications have been summarized and analysed. As shown in this paper, the HTS energy storage techniques have advantages for use in electrical power systems for improving the

power system operation capability and efficiency with power energy controls and improving the power system stability; and the technologies can be practically developed by using well developed HTS materials.

SFWES technology becomes suitable for practical applications with the special HTS advantages which normal techniques can not provide.

SMES technology was promoted and made great progress. Compared to another method of energy storage device, SMES has much better performances, firstly, the current density of SMES coil is about 10 or 100 times lager than the common coil, and the SMES coil carrying current operates at cryogenic temperature having virtually no resistive losses. Consequently, the energy can be stored in a persistent mode, until required to release. Secondly, the effective of SMES can get up to 95 % with energy exchange with power system within milliseconds, and SMES can be readily controlled. With the development of electronic technology, SMES can successfully enhance power system stability and improve the power quality through active and reactive power compensation. The major benefits of HTS SMES are: (i) High energy-storage efficiency, (ii) Fast energy charge (in a few milliseconds) and discharge capability, and (iii) Independent controllability of active and reactive power. In electric power industry, SMES systems can be used for load levelling, system stability enhancement, and fluctuating load compensation.

## References


[1] R. W. Boom, "Superconductive magnetic energy storage for electric utilities - A review of the 20 year Wisconsin program," *Proceedings of the International Power Sources Symposium*, Vol. 1, pp. 1-4, 1991.

[2] Z. J. Stekly, "Magnetic energy storage using superconducting coils," *Pulse Power Conference*, IDA/HQ 63-1412, pp. 53-58, 1996.

[3] J. X. Jin, L. H. Zheng, R. P. Zhao, J. Zhang, L. Jiang, J. H. Chen, Y. L. Jiang and H. Y. Zhang, "Summary of applied high temperature superconductivity," *Nature Sciences*, Vol. 1, No. 1, pp. 47-79, 2006.

[4] J. X. Jin, "Prototype of Bi-2223 coil," *Physica C*, Vol. 341-348, No. 1-4, pp. 2545-2546, 2000.

[3] T. Hardono, C. Cook and J. X. Jin, "Measurements of ac loss in HTSC wires exposed to an alternating field using calorimetric methods," *IEEE Transactions on Applied Superconductivity*, Vol. 9, No. 2, pp. 813-816, 1999.

[4] J. X. Jin, S. X. Dou and C. Grantham, "Parameters of Bi-2223/Ag high $T_c$ superconductor for electrical applications," *Proc. of 1998 International Conference on Power Electronic Drives and Energy Systems for Industrial Growth*, 1-3, Perth, Australia, pp. 930-935, 1998.

[5] Y. C. Guo, J. X. Jin, H. K. Liu, Y. Tanaka and S. X. Dou, "Long lengths of silver-clad Bi2223 superconducting tapes with high current-carrying capacity," *Applied Superconductivity*, Vol. 5, No. 1-6, pp. 163-170, 1997.

[6] J. X. Jin, C. Grantham, Y. C. Guo, J. N. Li, R. Bhasale, H. K. Liu and S. X. Dou, "Magnetic field properties of Bi-2223/Ag HTS coil at 77 K," *Physica C*, Vol. 278, pp. 85-93, 1997.

[7] J. X. Jin, S. X. Dou, H. K. Liu and C. Grantham, "High voltage generation with a high $T_c$ superconducting resonant circuit," *IEEE Transactions on Applied Superconductivity*, Vol. 7, No. 2, pp. 881-884, 1997.

[8] J. X. Jin, C. Grantham, H. K. Liu and S. X. Dou, "$(Bi,Pb)_2Sr_2Ca_2Cu_3O_{10+x}$ Ag-clad high-$T_c$ superconduct-ing coil and its magnetic field properties," *Philosophical Magazine B*, Vol. 75, No. 6, pp. 813-826, 1997.

[9] J. X. Jin, S. X. Dou, C. Grantham and H. K. Liu, "Preparation of high $T_c$ superconducting coils for consideration of their use in a prototype fault current limiter," *IEEE Transactions on Applied Superconductivity*, Vol. 5, No. 2, pp. 1051-1054, 1995.

[10] H. K. Liu, J. Yau, Y. C. Guo, Q. Y. Hu, J. X. Jin, N. Savvides and S. X. Dou, "Long Ag-clad Bi-based superconducting tapes and coils," *Physics B*, Vol. 194-196, pp. 2213-2214, 1994.

[11]S. X. Dou, H. K. Liu, Y. C. Guo, J. X. Jin and Q. Y. Hu, "Critical current density and irreversibility behaviour in Ag-sheathed Bi-based superconducting wires fabricated using a controlled melt procedure," *Applied Superconductivity*, Vol. 1, No. 10-12, pp. 1515-1522, 1993.

[12] P. F. Ribeir and M. L. Crow, "Energy storage systems for advanced power applications," *Proceedings of the IEEE: Applications of Superconductivity*, Vol. 89, No. 12, pp. 1744-1756, 2001.

[13] R. de Andrade Jr, A. C. Ferreira, G. G. Sotelo, W. I. Suemitsu, L. G. B. Rolim, J. L. Silva Neto, M. A. Neves, V. A. dos Santos, G. C. da Costa, M. Rosario, R. Stephan and R. Nicolsky, "A superconducting high-speed flywheel energy storage system," *Physica C*, Vol. 408-410, pp. 930-931, 2004.

[14] K. Liu, G. Wu and Y. L. Zhang, "Application and study of magnetic bearing flywheel technology," *Journal of Astronautics*, Vol. 26, No. 3, pp. 386-390, 2005.

[15] H. Zhang, Y. Kang and P. Liu, "Application and development of SMES in electric power system: Part two - Energy control equipment," *Automation of Electric Power Systems*, Vol. 25, No. 7, pp. 67-70, 2001.


Received: 20 July 2006/Revised: 31 January 2007

# A Phase Variable Model of Flyback Switching Converters Based on Numerical Magnetic Field Analysis Coupled With External Circuits

Jiaxin Chen[1,2], Youguang Guo[2] and Jianguo Zhu[2]
[1]College of Electromechanical Engineering, Donghua University, China
[2]Faculty of Engineering, University of Technology, Sydney, Australia

This paper presents a fast and accurate phase variable model of flyback switching converters. A modified dynamic circuit model of high frequency transformer, capable of including the effect of all types of core loss, is adopted. The dynamic differential inductances of the transformer are obtained based on nonlinear finite element magnetic field analysis. The developed phase variable model is implemented in Matlab/Simulink through variable inductance and variable core loss equivalent resistance to account for the winding current and voltage dependence. With this model, anomalous loss and natural output curve of flyback switching converters are investigated. This model has been applied to analyze an existing flyback converter and simulation results prove its practical merit and high effectiveness.

*Key Words*: Phase variable model, Flyback switching converter, Anomalous loss, Differential inductance, Finite element analysis.

## 1. Introduction

Because of its simpler structure than other types of switching mode converter, the flyback converter is commonly used as small power converter. To predict, assess and optimize the performance of flyback converters, a generalized dynamic simulation model for the behavior of flyback converters would always be useful. The flyback converter is composed of a transformer and external circuits, so the key issues for investigating its performance are the transformer modeling and the coupling between the transformer and external circuits.

As an accurate model, the transformer model must account for the nonlinear inductance and influence of all kinds of magnetic core loss. A generalized dynamic ladder network circuit model of high frequency transformer has been introduced in [1], [2] and the circuit model with one level of ladder network is shown in Fig. 1. Based on this model, this paper presents a more suitable model for the transformer as shown in Fig. 2. Due to the nonlinear magnetization property of soft magnetic cores, the differential inductance, $L_m$, varies with winding current, is obtained by nonlinear FE analysis. Using this winding current dependent parameter, a phase variable model of flyback converter is developed.

**Correspondence:** Youguang Guo, Faculty of Engineering, University of Technology, Sydney, PO Box 123, Broadway, NSW 2007, Australia,
email: youguang@eng.uts.edu.au.

In order to connect the transformer model and external circuits, the port voltage of each winding of transformer must be measured. A hybrid simulation model with two levels is built here. An adjustable differential inductance component is developed to represent the inductance dependence on the winding current. An adjustable core loss equivalent resistance component is also developed to represent the resistance dependence on the voltage across the inductance, $L_m$. By running this model in the Simulink environment, the comprehensive performance of a flyback switching converter could be obtained.

## 2. Modified Dynamic Model of High Frequency Transformer in Flyback Converters

### *2.1 Modified circuit model of transformer*

The model shown in Fig. 1 is capable of considering hysteresis loss, eddy current loss, anomalous loss and distributed capacitance. In the figure, $R_a$ is the nonlinear equivalent resistance of anomalous loss, $R_e$ is the equivalent resistance of eddy current loss, $L_m$ is the nonlinear differential inductance which has accounted for the effect of hysteresis loss, $R_P$ and $L_{PS}$ are the resistance and leakage inductance of the primary winding, $R'_{2s}$ and $L'_{2ss}$ are the equivalent resistance and equivalent leakage inductance of the secondary winding, respectively. The stray capacitance, $C_{str}$, can be obtained by experiment [2].

Since the soft magnetic cores used in flyback converters, such as TDK-PC40, have high electrical resistivity and narrow B-H hysteresis limiting loop, the skin effect, hysteresis loss and eddy current loss can be omitted. The main core loss is the anomalous loss, and the level number of the ladder circuit can be decreased to one as shown in Fig. 2. Considering the RCD (resistor, capacitor and diode) snub circuit in flyback converter has the similar function as the stray capacitance and the output power of the third winding is small, a modified dynamic circuit model of flyback switching converters is built and shown in Fig. 2.

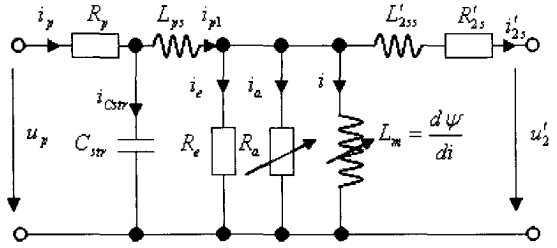


Fig. 1. Dynamic circuit model of transformer

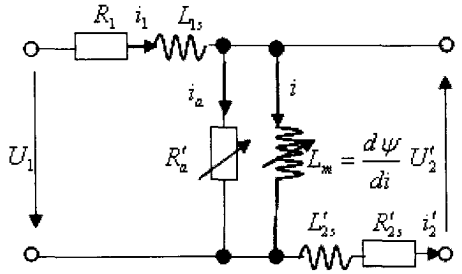


Fig. 2. Modified dynamic circuit model

## 2.2 Differential inductance

The winding differential inductances are calculated by the following steps: (1) For a given winding current, $i$, a non-linear field analysis is carried out to find the flux density in the core; (2) When the flux densities in two consecutive time steps (*e.g.* the $k$-th and $(k-1)$-th steps) are obtained, the differential inductances can be calculated by

$$L_m(i) = \frac{d\psi(k)}{di} = An_1 \frac{B(k) - B(k-1)}{i(k) - i(k-1)} \qquad (1)$$

where $A$ is the cross-sectional area of transformer core, $n_1$ is the number of turns of the primary winding, and $B$ is the flux density.

From (1), the differential inductance at different winding currents can be obtained and shown in Fig. 3. The leakage inductances, $L_{1s}$ and $L'_{2s}$, can be assumed as constant.

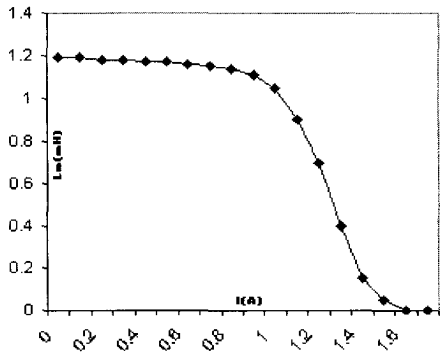


Fig. 3. Differential inductance with different winding currents

## 2.3 Consideration of anomalous loss

The anomalous loss $P_a$ of magnetic core can be obtained by [1]

$$P_a = C_a \left| \frac{dB}{dt} \right|^{3/2} \qquad (2)$$

where $C_a$ is the coefficient of anomalous loss.

Fig. 4 illustrates the core loss curves of FP40 provided by the manufacturer. By curve fitting, $C_a$ can be obtained.

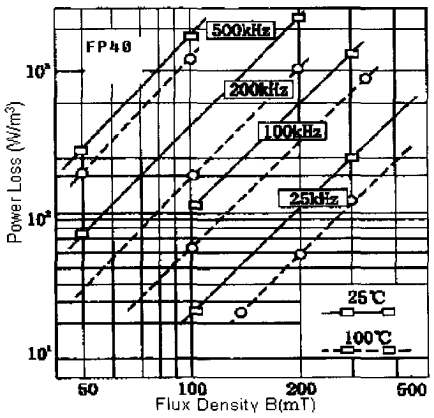


Fig. 4. Core loss curves of soft magnetic core - FP40

For a transformer with symmetrical structure, considering that the voltages across $R_1$ and $L_{1S}$ or $R'_{2s}$ and $L'_{2s}$ are very small comparing to $U_1$ and $U'_2$, the following equations can be obtained:

$$R'_a \approx \frac{(n_1 A)^{3/2}}{C_a w} |U_1|^{1/2}; \quad PWM = ON \qquad (3)$$

$$R'_a \approx \frac{(n_1 A)^{3/2}}{C_a w} |U'_2|^{1/2}; \quad PWM = OFF \qquad (4)$$

where $w$ is the mass of the core.

*2.4 Phase variable model*

The phase variable model for the transformer of flyback switching AC-DC converter is given as

$$U_1 = (R_1 i_1 + L_{1s}\frac{di_1}{dt}) + L_m\frac{di}{dt} \quad (5)$$

$$U_2' = -[(R_{2s}' i_2' + L_{2s}'\frac{di_2'}{dt}) + L_m\frac{di}{dt}] \quad (6)$$

$$i = i_1 + i_2' - L_m\frac{di}{dt}/R_a' \quad (7)$$

where $L_{1s}$, $L_m$ and $L'_{2s}$ can be obtained from the nonlinear FE solutions, in which the saturation effect is considered, and $R'_a$, which relies on the voltage across $L_m$, is obtained from (2)-(4).

## 3. Dynamic Simulation Model for Flyback Switching DC-DC Converters

Based on the analysis and circuit models obtained in Section 2, the hybrid dynamic simulation model for flyback switching DC-DC converters is built. It has two level structures: the top level is a digital system instituted by all the switching parts and some other pure parts with switching characteristic, and the second level is a continuous system instituted by all passive components.

*3.1 Simulation model of transformer*

According to (2)-(4), the anomalous loss coefficient $C_a$ and the equivalent loss resistance $R'_a$ can be obtained. $C_a$ is determined as 5 x $10^{-5}$. $R'_a$ relies on the winding current and voltage and its corresponding simulation block is a MATLAB function. The differential inductance $L_m$ can be obtained by the method of look-up table, in which the data of differential inductance versus current have been preset. As there is a RCD circuit in the primary winding, the stray capacitance of $C_{str}$ can be omitted here. Fig. 5 shows the simulation model of transformer considering anomalous loss and differential inductance.

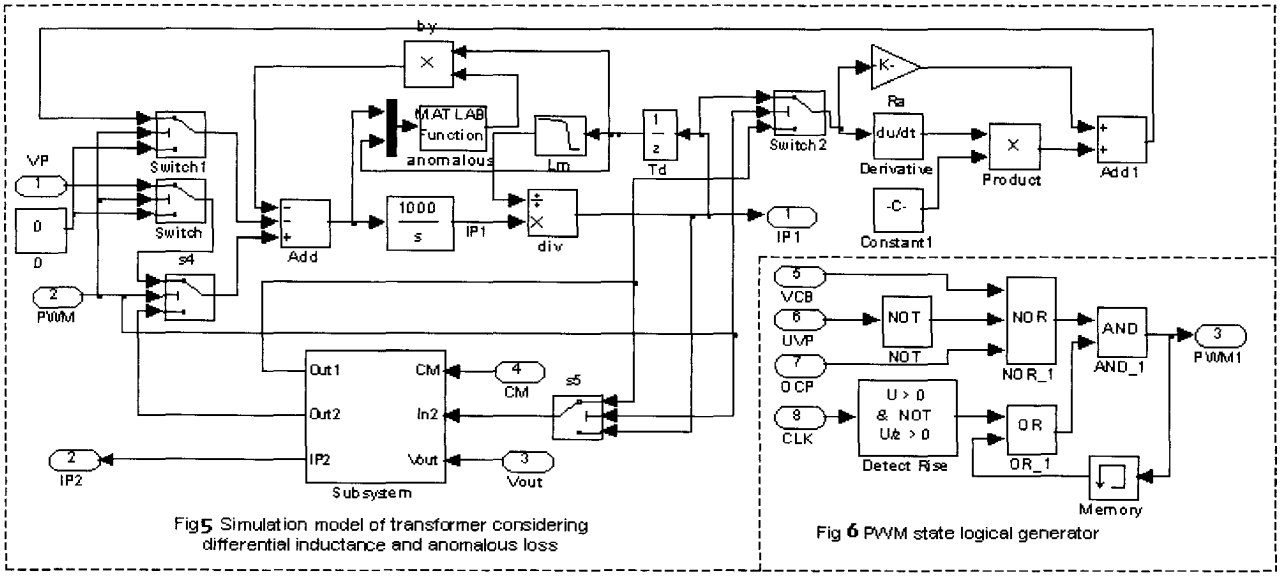


Fig5 Simulation model of transformer considering differential inductance and anomalous loss

Fig 6 PWM state logical generator

*3.2 Pulse width modulation (PWM)*

According to the principle of flyback switching converters, the PWM state is decided by

$$PWM^{n+1} = (CLK\uparrow + PWM^n) \overline{\&\ (VCB^n + \overline{UVP}^n + OCP^n)} \quad (8)$$

where VCB is the logical state of output voltage, which is true when the output voltage is larger than the rated, otherwise false; UVP is the logical state of UC3842, which is true when the UC3842 works and produces a PWM signal, otherwise false; OCP is the logical state of over current protection, which is true when the UC3842 operates in the over current protection mode, otherwise false; and CLK↑ is the rise of time clock. The corresponding simulation model is shown in Fig. 6. Based on (1)-(8), the complete simulation model of flyback converter is obtained.

## 4. Simulation of an Existing Converter

The simulation model is applied to analyze an existing flyback DC-DC converter, as shown in Fig. 7. The major parameters include: input voltage of 102-370 VDC, nominal output voltage

of 5 VDC, rated output current of 3.6 A, and switching frequency of 60 kHz. The transformer is E25/FP40. By using the proposed model, some performances of the converter are obtained.

Fig. 8(a) illustrates the simulated operation process of the converter with the rated load when $V_{in}$=102 VDC, and Fig. 8(b) plots the enlarged steady state. The simulation results show that the basic nominal requirements of the converter can be met. According to Figs. 9 and 10, it can be seen that when the input voltage rises, the output capacity and anomalous loss increase if the output keeps constant, *e.g.* the rated load.

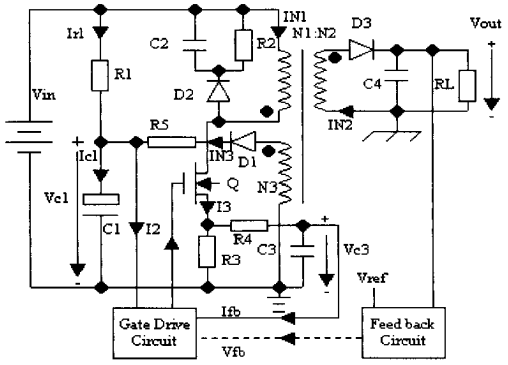


Fig. 7. Circuit topology of the flyback converter

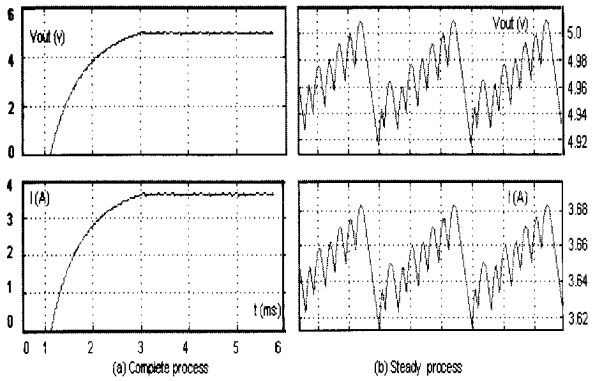


Fig. 8. Simulation results by using the phase variable transformer model with the rated load.

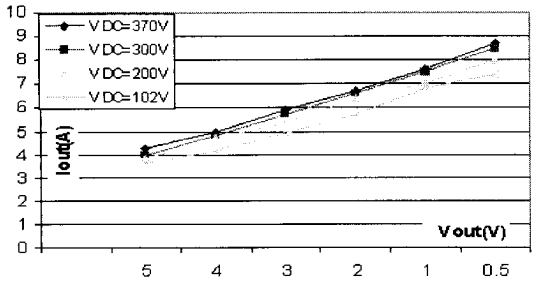


Fig. 9. Natural output curves of flyback converter at different input voltages.

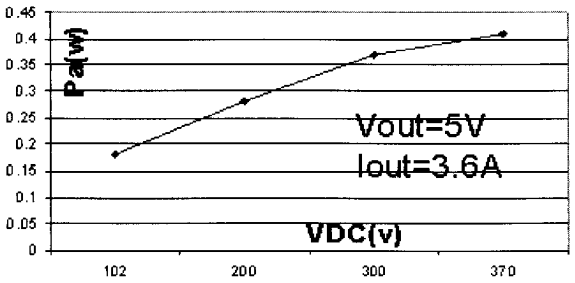


Fig. 10. Anomalous loss at different input voltages

## 5. Conclusion

This paper presents a generalized dynamic model for flyback switching DC-DC converters. In this model, a modified phase variable transformer model and several important factors are taken into account. The systematic method to build the hybrid model - system switching state based on time sequence is also introduced. The proposed simulation model is implemented in MATLAB/Simulink and applied to analyze an existing flyback DC-DC converter. The model is verified by the simulation results.

## References

[1] J. G. Zhu and V. S. Ramsden, "A generalized dymanic circuit model of magnetic cores for low- and high-frequency application - Part I: theoretical calculation of the equivalent core loss resistance," *IEEE Trans. Power Electronics*, Vol. 11, No. 2, pp. 246-250, 1996.

[2] H. Y. Lu, J. G. Zhu and V. S. Ramsden, "Dynamic circuit modeling of a high frequency transformer," *Proc. IEEE Power Electronics Specialists Conf.*, Fukuoka, Japan, pp. 1497-1485, 1998.

[3] J. X. Chen, J. G. Zhu, Y. G. Guo and J. X. Jin, "Modeling and simulation of flyback DC-DC converter under heavy load," *Proc. Int. Conf. on Communication, Circuits and Systems*, Guilin, China, pp. 2752-2756, 2006.

[4] J. X. Chen, "Energy self-holding in flyback switching DC-DC converters," *Proc. Int. Conf. Electrical Machines and Systems*, Nanjing, China, pp. 1194-1197, 2005.

Received: 20 July 2006/Revised: 31 January 2007

# Comprehensive Performance Evaluation of a High Speed Brushless DC Motor Using an Improved Phase Variable Model

Jiaxin Chen[1,2], Youguang Guo[2] and Jianguo Zhu[2]
[1]College of Electromechanical Engineering, Donghua University, China
[2]Faculty of Engineering, University of Technology, Sydney, Australia

This paper presents the performance evaluation of a high-speed surface mounted PM brushless DC motor by using an improved phase variable model. Magnetic field finite element analyses are conducted to accurately calculate the key motor parameters such as air gap flux, back electromotive force and inductance, and their dependence on rotor position and magnetic saturation. Based on the numerical magnetic field solutions, a modified incremental energy method is applied to effectively calculate the self and mutual inductances of the stator windings. In order to evaluate the comprehensive performance of the motor, especially the motor output at high-speed operation, which is affected by the dynamic inductances, an improved phase variable model is derived to simulate the motor performance. In the model, the rotor position dependence of key parameters is taken into account. The motor prototype has been constructed and tested with both a dynamometer and a high-speed embroidery machine, validating successfully the theoretical calculations.

*Key Words*: BLDC motor, Performance evaluation, Finite element analysis, Improved phase variable model.

## 1. Introduction

High speed permanent magnet (PM) motors with brushless DC (BLDC) control scheme have found wide applications in industrial and domestic appliance drive market because of their advantages such as high efficiency, high power density and high drive performance [1]-[3]. This paper presents the performance analysis of a surface mounted PM BLDC motor for driving high-speed embroidery machines by using an improved phase variable model. In the design of the motor, magnetic field finite element analysis (FEA) was conducted to accurately calculate key motor parameters such as air gap flux, back electromotive force (*emf*), and inductance, and cogging torque, etc. Based on the numerical magnetic field solution, a modified incremental energy method is applied to effectively calculate the self and mutual inductances of the stator windings.

The rise rate of armature current is limited by the winding inductances, and this may affect the output performance of the motor, especially when operating at high speed. Therefore, it is necessary to investigate whether or not the motor can reach the required electromagnetic torque and speed at a given voltage. Based on [4], an improved phase variable model [5] is developed and implemented in the Matlab/Simulink environment for evaluating the motor's dynamic and steady state performance. In the model, the real waveforms of back *emf* and inductances are taken into account.

The developed motor prototype has been fabricated and tested with both a dynamometer and a high-speed embroidery machine. Experimental results verify the theoretical analyses.

## 2. Motor Structure and Major Dimensions

Fig. 1 illustrates the magnetically relevant parts of the motor prototype. The laminated stator has 12 slots, in which the three phase single-layer windings are placed (not shown for clarity). The rotor core and shaft are made of solid mild steel, and four pieces of NdFeB PMs are mounted and bound on the surface of the rotor. The stator core has an inner diameter of 38 mm, outer diameter of 76 mm, and axial length of 38 mm. The main air gap length and the height of PMs along the radial magnetization direction are chosen as 1 mm and 2.5 mm, respectively. The motor is designed to deliver an output torque of 1.0 Nm at a speed of not less than 5000 rev/min.

**Correspondence:** Youguang Guo, Faculty of Engineering, University of Technology, Sydney, PO Box 123, Broadway, NSW 2007, Australia,
email: youguang@eng.uts.edu.au.

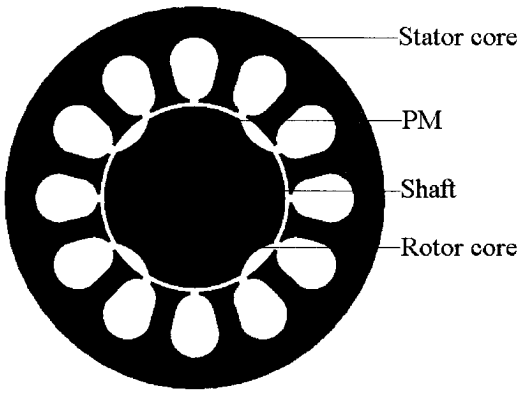


Fig. 1. Cross section of a PM BLDC motor

## 3. Parameter Computation

### *3.1 Winding flux, back emf, and cogging Torque*

Magnetic field FEA can take into account the detailed structure and dimensions of the motor and the non-linearity of ferromagnetic materials, and hence can accurately compute the motor parameters and performance [6]. Fig. 2 illustrates the plot of magnetic flux density vectors at no-load at $\theta$=0°, *i.e.* the rotor position shown in Fig. 1. From the no-load field distribution, the PM flux (defined as the flux of one coil produced by the rotor PMs), back *emf* of one phase winding, and cogging torque can be determined. The curves of these parameters against the rotor angular position or time can be obtained by a series of magnetic field FEAs at different rotor positions. Fig. 3 shows the no-load flux linking a coil (two coils form a phase winding) at different rotor positions. By applying the discrete Fourier transform, the magnitude of the fundamental of the coil flux was calculated as $\phi_1$=0.543 mWb, and the *emf* constant can then be determined as 0.2457 Vs/(mech rad), by

$$K_E = \frac{p}{2} N_s \frac{\phi_1}{\sqrt{2}} \tag{1}$$

where $p$=4 is the number of poles and $N_s$=320 the number of turns of a phase winding. The torque constant can be obtained by $K_T$=$mK_E$, where $m$=3 is the number of phases.

From the no-load magnetic field distribution, the cogging torque curve can also be calculated by the Maxwell stress tensor method, or the virtual work method. It was found that the cogging torque of this surface-mounted PM motor is very small with a maximum value of 0.014 Nm.

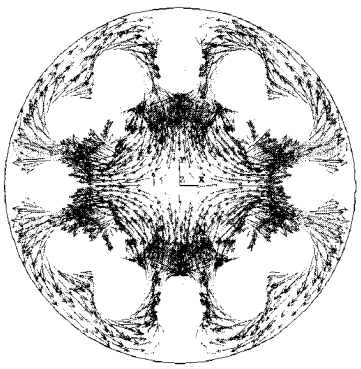

Fig. 2. Plot of no-load magnetic flux density vectors

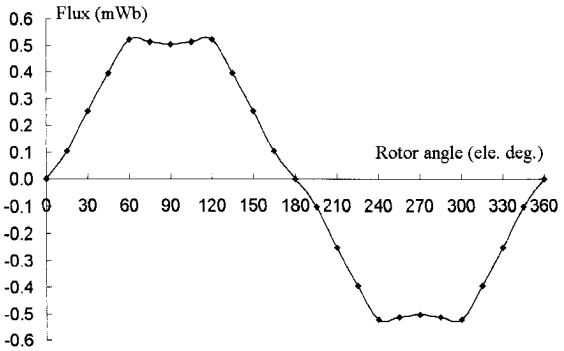


Fig. 3. PM Flux per turn versus rotor angle

### *3.2 Winding Inductance*

The behavior of the motor equivalent electrical circuit is dominated by the incremental inductance rather than the apparent inductance. In this paper, the winding incremental inductances are calculated by a modified incremental energy method [7], which includes the following steps: (1) For a given rotor position $\theta$, conduct a non-linear field analysis considering the saturation due to the PMs to find the operating point of the motor, and save the incremental permeability in each element; (2) Set the remanence of PMs to be zero, and conduct linear field analyses with the saved permeabilities under perturbed stator current excitations, *i.e.* assigning the 3 phase winding currents as $(i_a,i_b,i_c)$ = $(\Delta i,\Delta i,0)$, $(\Delta i,0,\Delta i)$, $(0,\Delta i,\Delta i)$, $(\Delta i,0,0)$, $(0,0,\Delta i)$, and $(0,\Delta i,0)$, respectively; (3) Calculate the magnetic co-energy for each current excitation; and (4) Calculate the incremental inductances by

$$L_{aa}(\theta) = L_{bb}(\theta) = L_{cc}(\theta) = \frac{2W_c(\Delta i,0,0,\theta)}{(\Delta i)^2} \tag{2a}$$

$$L_{ab}(\theta) = L_{ba}(\theta) = \frac{W_c(\Delta i,\Delta i,0,\theta) - W_c(0,\Delta i,0,\theta) - W_c(\Delta i,0,0,\theta)}{(\Delta i)^2} \tag{2b}$$

$$L_{bc}(\theta) = L_{cb}(\theta) = \frac{W_c(0,\Delta i,\Delta i,\theta) - W_c(0,\Delta i,0,\theta) - W_c(0,0,\Delta i,\theta)}{(\Delta i)^2} \quad (2c)$$

$$L_{ca}(\theta) = L_{ac}(\theta) = \frac{W_c(\Delta i,0,\Delta i,\theta) - W_c(0,0,\Delta i,\theta) - W_c(\Delta i,0,0,\theta)}{(\Delta i)^2} \quad (2d)$$

Fig. 4 shows the calculated self and mutual incremental inductances at different rotor positions.

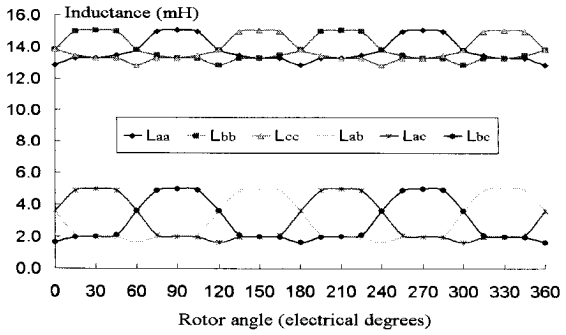


Fig. 4. Winding inductances versus rotor angle

## 4. Improved Phase Variable Model

The equation-based phase variable model of BLDC motor is given as

$$V_{abc} = r_{abc} i_{abc} + \frac{d\psi_{abc}}{dt} + e_{abc} \quad (3)$$

$$\psi_{abc} = L_{abc} i_{abc} \quad (4)$$

$$T_m = \frac{e_a i_a + e_b i_b + e_c i_c}{\omega_r} + T_{cog} \quad (5)$$

$$J\frac{d\omega_r}{dt} = T_m - B\omega_r - T_L \quad (6)$$

$$L_{ab} = L_{ba},\ L_{bc} = L_{cb},\ L_{ca} = L_{ac},\ r_a = r_b = r_c \quad (7)$$

$$i_a + i_b + i_c = 0 \quad (8)$$

All above variables are used as their conventional meanings. The profiles of $L_{abc}$, $e_{abc}$, and $T_{cog}$ are obtained from the nonlinear time-stepping FEA solutions, in which the rotor position dependence and saturation effect are considered.

For dynamic performance evaluation, compared with an equivalent electric circuit model, the nonlinear time-stepping magnetic field FEA can give accurate results but is more time consuming. A phase variable model of BLDC motor based on FEA coupling with external circuits, which behaves much faster with the same level of accuracy, has been introduced and verified in [4]. However, the equation-based model cannot be applied to BLDC motors directly, so an additional model composed of several circuit components has to be employed.

In [5], we proposed a pure mathematical method to work out the central point potential (voltage) of the Y-connected three phase symmetrical windings, so that the port voltages of all phase windings in both energized and non-energized conditions can be estimated. In this way, the improved phase variable model can be directly applied to investigate the performance of BLDC motors.

## 5. Performance Simulation and Validation

The basic design requirement for the motor drive system is that for an output torque of 1.0 Nm, the steady-state speed should be no less than 5000 rpm when the inverter DC bus voltage is $V_{dc}$=310 VDC. By using the proposed model, the motor drive system is simulated under these conditions and some of the results are plotted in Figs. 5-8, showing that the motor can meet the design requirements.

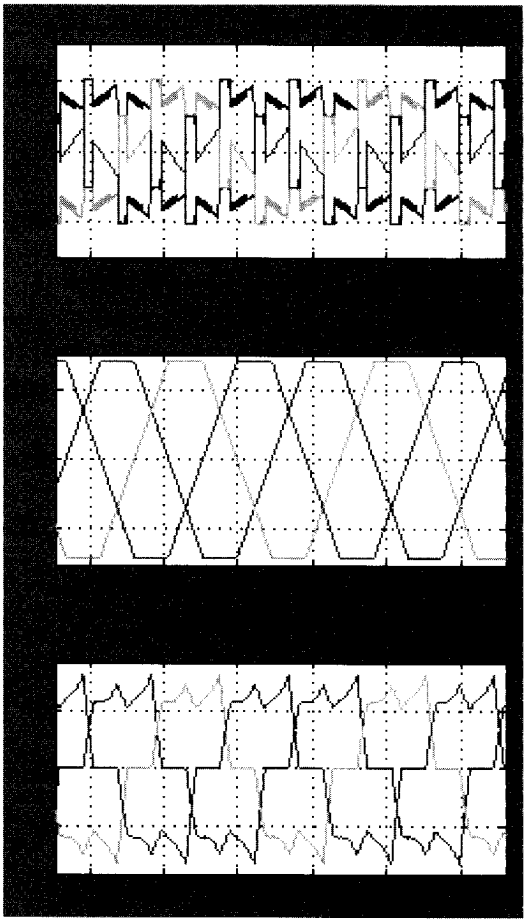

Fig. 5. Simulated steady performance

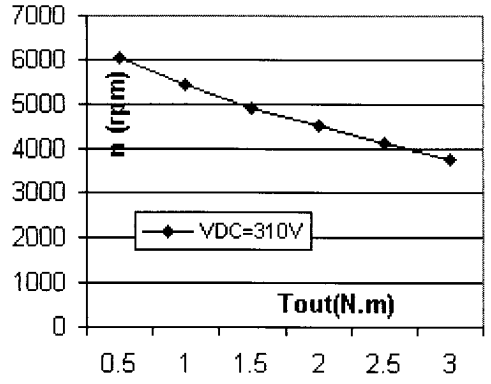


Fig. 6. Curve of steady speed versus output torque

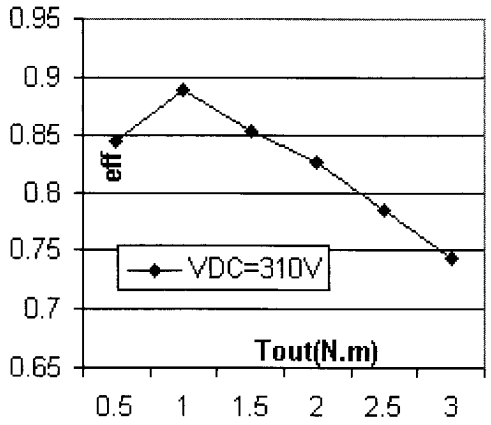


Fig. 7. Curve of motor efficiency versus output torque

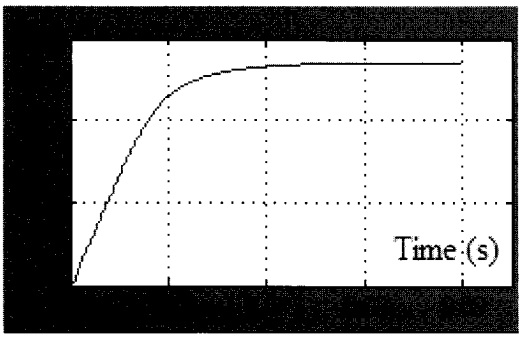


Fig. 8. Speed curve during start-up with $T_L$=1.0 Nm and $V_{in}$=310 VDC

The designed motor has been fabricated and successfully operated with a brushless DC control scheme. Experiments have been conducted on the prototype. The back *emf*, for example, was measured at different rotor speeds and the experimentally determined *emf* constant is 0.2464 Vs/rad, which is very close to the theoretical value. Other parameters, such as the inductances and torque/speed curves are also in substantial agreement with the theory.

## 6. Conclusion

This paper presents the comprehensive performance evaluation of a high-speed permanent magnet brushless DC motor by an improved phase variable model, which is implemented in Simulink surrounding. The rotor dependence and magnetic saturation effect on key motor parameters such as back *emf* and inductances are considered.

For accurate computation of the motor parameters, nonlinear time-stepping finite element magnetic field analysis is performed and improved formulations, *e.g.* a modified incremental energy method for calculating the self and mutual winding inductances, are employed.

The motor has been constructed and tested with a brushless DC control scheme, validating the theoretical design and analysis.

## References

[1] T. Kenjo, *Permanent Magnet and Brushless DC Motors*, Oxford University Press, 1985.

[2] J. Shao, D. Nolan, M. Teissier and D. Swanson, "A novel microcontroller-based sensorless brushless DC (BLDC) motor drive for automotive fuel pumps," *IEEE Trans. Industry Applications*, Vol. 39, No. 6, pp. 1734-1740, 2003.

[3] G. Jang and M.G. Kim, "A bipolar-starting and unipolar-running method to drive a hard disk drive spindle motor at high speed with large starting torque," *IEEE Tran. Magn.*, Vol. 41, No. 2, pp. 750-755, 2005.

[4] O. A. Mohammed, S. Liu and Z. Liu, "A phase variable model of brushless dc motors based on finite element analysis and its coupling with external circuits," *IEEE Tran. Magn.*, Vol. 41, No. 5, pp. 1576-1579, 2005.

[5] J. X. Chen, Y. G. Guo and J. G. Zhu, "Improved phase variable model and field-circuit coupling method for performance analysis of high speed PM brushless DC motor," *Asia-Pacific Symposium on Applied Electromagnetics*, Sydney, Australia, 2006, Full paper accepted for publication in *Journal of Japanese Society of Applied Electromagnetics and Mechanics*.

[6] Y. G. Guo, J. G. Zhu, P. A. Watterson and W. Wu, "Development of a permanent magnet transverse flux motor with soft magnetic composite core," *IEEE Trans. Energy Conversion*, Vol. 21, No. 2, pp. 426-434, 2006.

[7] Y. G. Guo, J. G. Zhu and H. Y. Lu, "Accurate determination of parameters of a claw pole motor with SMC stator core by finite element magnetic field analysis," *IEE Proceedings – Electric Power Application*, Vol. 153, No. 4, pp. 568-574, 2006.

Received: 20 July 2006/Revised: 31 January 2007

# A Permanent Magnet Synchronous Motor Model with Core Loss

Ying Yan, Jianguo Zhu and Youguang Guo
Faculty of Engineering, University of Technology, Sydney, Australia

This paper presents an improved model of permanent magnet synchronous motors (PMSMs) considering core losses. The core losses of a surface mounted PMSM were measured at no-load and load, and the analysis on experimental results shows that the core losses in a PMSM can be attributed to the components produced by the rotor permanent magnets and the stator currents. The conventional equivalent circuit model of PMSM with core loss can account for the former but not the latter, and therefore, an additional core loss resistor is required to account for the additional core loss component due to the armature reaction. The nonlinear resistance for the no-load core loss is explained from the core loss model of magnetic materials. The method to determine these core loss resistances from the no-load and load tests is also presented. The relation between the core loss components and the corresponding resistors is clearly demonstrated by the analysis of experimental results.

*Key Words:* Permanent magnet synchronous motor model, Core loss

## 1. Introduction

The permanent magnet synchronous motor (PMSM) can be a serious competitor to the conventional DC and induction motors in servo applications due to its high power density, torque to current ratio, and efficiency. The model of PMSM is concerned by many researchers because it is important in motor performance analysis and drive system design. In addition, the performance of a PMSM drive system is considerably influenced by the accuracy of the model.

The core loss or iron loss, caused by the permanent magnet (PM) flux and armature reaction flux, is a significant component in the total loss of a PMSM, and thus, it can have a considerable effect on the PMSM modeling and performance prediction. This paper proposes a model of PMSM taking into account the stator core losses. No-load and load tests were carried out to determine the total core and mechanical loss of a PMSM, which was then separated by fitting the experimental results to their physical models. The relationship between the core loss resistor $R_{c1}$ and the internal voltage $V_i$ is estimated by the curve fitting of the no-load results. With the load test results, the conventional PMSM model is modified by adding an extra resistor, $R_{c2}$, to account for the effect of armature reaction on the core loss. The values of $R_{c2}$ are determined by the analysis of the PMSM operational states. Finally, the modified equivalent circuit and the core loss mechanisms are discussed.

**Correspondence:** Ying Yan, Faculty of Engineering, University of Technology, Sydney, PO Box 123, Broadway, NSW 2007, Australia, email: yingyan@eng.uts.edu.au.

## 2. Experimental Study of Core Losses in PMSM

The core losses of a surface mounted PMSM were measured with and without load. In order to obtain the core loss, some electrical and magnetic parameters of the motor, such as the magnetizing flux linkage produced by rotor PMs, stator winding resistance and inductances are required. Experiments are firstly conducted to measure these parameters.

The magnetizing flux linkage $\lambda_m$ is obtained by measuring the phase voltage by the open circuit test, and the synchronous inductance $L_{syn}$ is measured by the short circuit test. In order to find out the leakage inductance $L_l$, the mutual inductance, $L_m$, between different phases is measured by exciting one of the three phases of the motor. The experimental results are: $\lambda_m$ = 0.118 Wb, $L_{syn}$ = 12.8 mH, $L_m$ = 3.29 mH. The stator winding resistances at various temperatures are measured by the V-A method in an environmental chamber. The relationships between the phase resistances and motor temperature are obtained as: $R_U$ = 1.579(1+0.004033$T$), $R_V$ = 1.584 (1+0.004017$T$), and $R_W$ = 1.602(1+0.003946$T$), where $T$ is the temperature in Celsius.

### *2.1 No-load test*

The test system for measuring the core losses contains the PMSM and a DC motor coupled with a torque meter. The PMSM, as a generator, is driven

by the DC motor at various speeds by adjusting the armature voltage of the DC motor. Through a power flow analysis, the following power balance equation can be obtained

$$P_{in} = P_{Cu} + P_c + P_{mech} + P_{out} \quad (1)$$

where the input power $P_{in} = T_m\omega_r$, $T_m$ is the measured shaft torque, $\omega_r$ the angular speed, and the copper loss $P_{Cu} = \Sigma I^2R$. Under no load, the output power $P_{out} = 0$, and therefore, the sum of the core loss $P_c$ and mechanical loss $P_{mech}$ can be obtained by $P_c+P_{mech} = P_{in}-P_{Cu}-P_{out}$. Fig. 1 shows the experimental result of $(P_c+P_{mech})$ versus rotor speed in rpm.

### 2.2. Load test

Further experiment is carried out to investigate the core loss of a PMSM operated as a generator with different load currents. The test system is similar to that for the no-load test. Various resistive loads, such as 20, 30, 40, 50, 60, 75, 90, and 110 Ω, are connected to the PMSM, respectively. The experimental results of mechanical and core losses at various loads are also illustrated in Fig. 1.

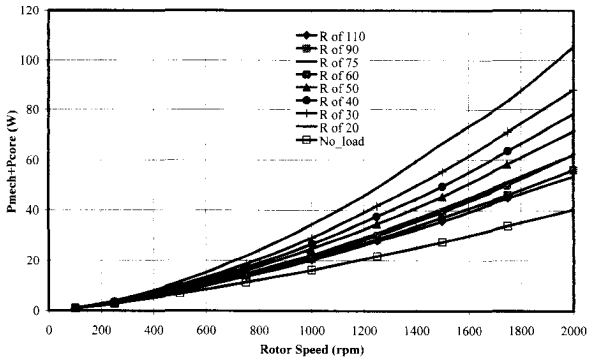


Fig. 1. $(P_c+P_{mech})$ measured by no-load and load tests

## 3. Conventional Core Loss Models

### 3.1 Core losses in magnetic materials

In a soft magnetic material, the total core loss $P_c$ can be separated into hysteresis loss $P_h$ and eddy current loss, which in practice can be calculated in terms of the classical eddy current loss, $P_e$, and the anomalous loss, $P_a$, and can be expressed as follows [1], [2].

$$P_c = P_h + P_e + P_a \quad (2)$$

Under the excitation of a circular rotating field in the steady state, it can be expressed as

$$P_c = P_{hr} + 2C_e(fB)^2 + C_a(fB)^{3/2} \quad (3)$$

where $B$ is the peak value of the flux density vector, $f$ the frequency, $C_e$ and $C_a$ are the coefficients which can be determined by experiment, and $P_{hr}$ the rotational hysteresis loss.

### 3.2 Conventional model of PMSM with core losses

Among the power losses in a PMSM, the core loss $P_c$ is a significant but difficult component to determine. Fig. 2 illustrates a per-phase equivalent circuit of PMSM commonly used to account for the core loss [3], [4].

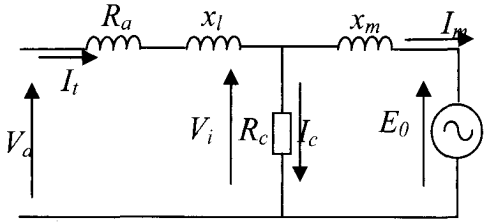


Fig. 2. Per-phase equivalent circuit with core loss

### 3.3 Curve fitting of experimental results under no-load condition

The mechanical loss and the core loss measured under no-load can be separated by the following method. The mechanical loss is generally a function of the rotor speed, and can be expressed as $P_{mech} = a_1\omega_r+a_2\omega_r^2+ a_3\omega_r^3$, where $a_1$, $a_2$, and $a_3$ are constant coefficients. The core loss, on the other hand, can be related to the internal voltage $V_i$, which is proportional to the product of frequency and magnetizing flux linkage, *i.e.* $f\lambda_m$, or $fB$ since $\lambda_m$ is proportional to $B$. Therefore, considering (3) and $P_{hr} = C_hfB^h$, where $h$ is a constant, we have

$$P_c + P_{mech} = C_h f^{1-h}V_i^h + C_eV_i^2 + C_aV_i^{3/2} + a_1\omega_r + a_2\omega_r^2 + a_3\omega_r^3 \quad (4)$$

The coefficients in (4) can be determined by the least square curve fitting of the experimental results, and hence the mechanical and core losses can be mathematically separated. From the no-load test results in Fig. 1, these coefficients are determined as: $C_h = 1.00\times10^{-8}$, $h = 1.8$, $C_e=1.582\times10^{-5}$, $C_a = 3.795\times10^{-2}$, $a_1 = 1.516\times10^{-1}$, $a_2 = 2.727\times10^{-5}$, and $a_3 = 6.075\times10^{-7}$. Fig. 3 plots the separated core and mechanical losses versus rotor speed.

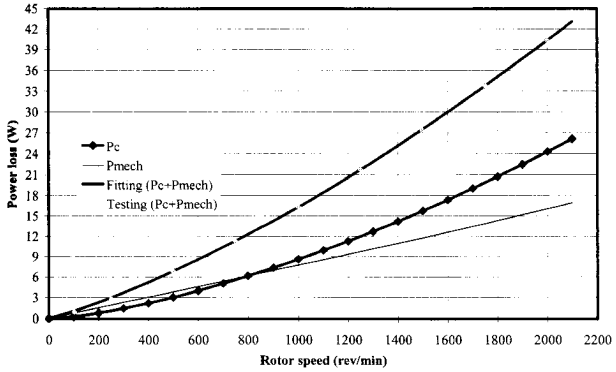


Fig. 3. Separation of no-load mechanical and core losses

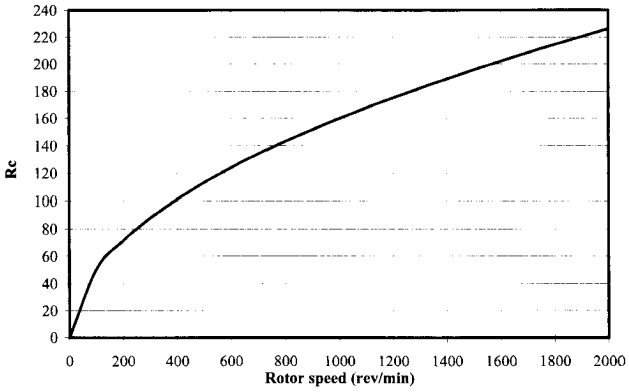


Fig. 4. Core loss resistance versus speed

The core loss resistor $R_c$ is then calculated by

$$R_c = 3V_i^2 / P_c \tag{5}$$

using the core loss obtained by the loss separation procedure, and the result is plotted in Fig. 4.

Since the motor flux density and rotor speed are reflected by the internal voltage $V_i$ under the no-load condition, $R_c$ can be expressed as a function of $V_i$. As it varies significantly with respect to the flux density distribution in the motor, which affects $V_i$, the core loss resistance $R_c$ cannot be regarded as a constant.

## 4. Core Loss Model of PMSM with Load

When the PMSM is loaded, the field distribution is distorted by the stator currents, which generate an extra component of core loss as illustrated by the experimental results in Fig. 1. To account for the core loss component due to stator currents, an extra resistor $R_{c2}$ was added to the per-phase equivalent circuit, as shown in Fig. 5 [4].

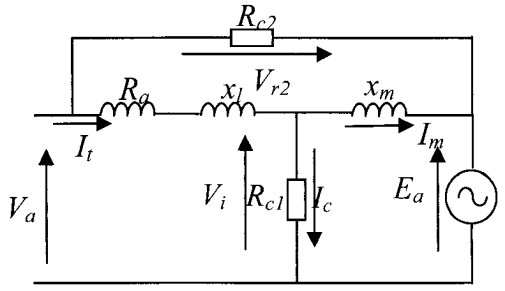


Fig. 5. Per-phase equivalent circuit considering core loss

In order to calculate the core loss resistor $R_{c2}$, the additional core loss component $P_{c2}$ caused by armature reaction is obtained by subtracting the mechanical and core losses under no-load from those losses measured in the load testing. From the equivalent circuit shown in Fig. 5, we have

$$V_{r2} = E_a \cos\delta + jE_a \sin\delta - V_a \tag{6}$$

$$E_a = \omega\lambda_m \tag{7}$$

$$R_{c2} = 3V_{r2}^2 / P_{c2} \tag{8}$$

where $V_{r2} = V_a - E_a$ is the voltage across $R_{c2}$, $\omega$ the rotor speed in electrical rad/s, and $\delta$ the load angle. By neglecting the stator resistance, the load angle can be approximately estimated by

$$\sin\delta = \frac{P_{em}X_s}{3E_aV_a} \tag{9}$$

where $P_{em}$ is the electromagnetic power obtained by subtracting the mechanical loss from the input power, and $X_s$ the synchronous reactance.

Fig. 6 plots the additional core loss, $P_{c2}$, at different $V_{r2}$ and rotor speeds, and Fig. 7 the calculated $R_{c2}$ with respect to $V_{r2}$ at different speeds. It is shown that both the additional core loss, $P_{c2}$, due to the armature reaction and the corresponding resistor, $R_{c2}$, are proportional to $V_{r2}$ and independent of the rotor speeds.

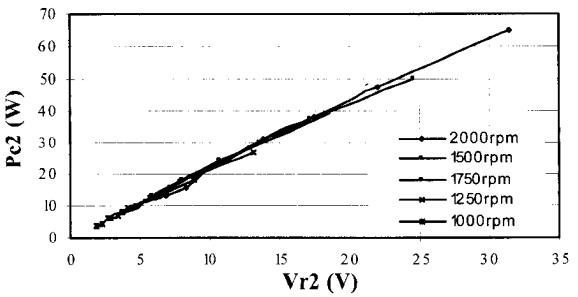


Fig. 6. Measured $P_{c2}$ versus $V_{r2}$ at different rotor speeds

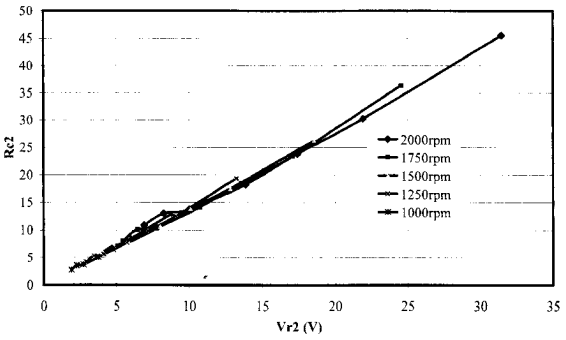


Fig. 7. $R_{c2}$ versus $V_{r2}$ at different rotor speeds

## 5. Discussion

In a PMSM, the total flux is composed of the fluxes produced by the rotor PMs and the stator currents. The finite element magnetic field analysis reveals that the magnetic field produced by the rotor PMs is distorted by the stator current flux, to some degree, and the distortion effects, such as saturation and demagnetization, vary with the stator current and rotor position. On the other hand, the load testing results show that the additional core losses caused by the stator flux cannot be simply represented by the variation of the internal voltage. This can also be observed from Figs. 6 and 7 as the variation of internal voltage, $V_i$, does not have effect on the additional core loss component and the corresponding resistance.

## 6. Conclusions

As revealed by the analysis of the experimental results of the no-load and load tests, the core loss in a PMSM can be attributed to the components produced by the rotor PMs (the no-load stator core loss) and the stator currents (the additional core loss component under load). The conventional equivalent circuit model of PMSM with core loss can account for the former but not the latter, and therefore, an additional core loss resistor is introduced to consider the addition core loss component due to the armature reaction. The nonlinear resistance for the no-load core loss is explained from the core loss model of magnetic materials. The method to determine these core loss resistances from the no-load and load tests is also presented. The relation between the core loss components and the corresponding resistances is demonstrated by the analysis of experimental results.

## References

[1] J. G. Zhu, "Numerical modelling of magnetic materials for computer aided design of electromagnetic devices," *Ph.D Thesis*, University of Technology, Sydney, 1994.

[2] H. Y. Lu, "Numerical simulation of high frequency transformers in power electronic systems," *Ph.D Thesis*, University of Technology, Sydney, 2001.

[3] A. H. Wijenayake and P. B. Schmidt, "Modeling and analysis of permanent magnet synchronous motor by taking saturation and core loss into account," *Proc. of International Conference on Power Electronics and Drive Systems*, Singapore, pp. 530-534, 1997.

[4] A. Consoli and G. Renna, "Interior type permanent magnet synchronous motor analysis by equivalent circuits," *IEEE Transactions on Energy Conversion*, Vol. 4, No. 4, pp. 681-689, 1989.

Received: 20 July 2006/Revised: 31 January 2007

# Improved Phase Variable Model and Field-Circuit Coupling Method for Performance Analysis of High Speed PM Brushless DC Motor

Jiaxin Chen[1,2], Youguang Guo[2] and Jianguo Zhu[2]
[1]College of Electromechanical Engineering, Donghua University, China
[2]Faculty of Engineering, University of Technology, Sydney, Australia

This paper presents an improved phase variable model and field-circuit coupling method to evaluate the comprehensive performance of brushless DC (BLDC) motors in both steady and dynamic conditions. In the proposed model, major motor parameters such as inductances, back electromotive force and cogging torque are obtained based on time-stepping nonlinear finite element analyses. The phase variable model is built and implemented in the MATLAB/Simulink through look-up tables to decide the rotor position dependence of the parameters. Furthermore, a mathematical method is proposed for determining the central point voltage of the Y-connected three phase windings, so that the model can obtain the input voltages of both energized and non-energized phase windings, and can be directly applied to BLDC motors. By using the developed model, the comprehensive performance of a high-speed surface mounted permanent magnet BLDC motor prototype is investigated.

*Key Words:* Improved phase variable model, Field-circuit coupling, BLDC motor, Performance evaluation.

## 1. Introduction

Thanks to the advantages such as high efficiency, high power density and high drive performance, permanent magnet (PM) brushless DC (BLDC) motors have been widely applied in industrial and domestic appliances [1]. As a crucial part in the electrical driving system design, a fast and accurate model for predicting, assessing and optimizing the performance of BLDC motors would be always useful.

For performance evaluation, compared with an equivalent electrical circuit model, the time-stepping nonlinear magnetic field finite element analysis (FEA) can provide accurate results but is more time consuming. A phase variable model of BLDC motor based on FEA and coupled with external circuits, which behaves much faster with the same level of accuracy, has been introduced and verified in [2], [3]. In the model, the inductances, back electromotive force *(emf)* and cogging torque were obtained by nonlinear FEA. However, the equation-based model cannot be applied to BLDC directly and a model composed of several circuit components has to be employed. To solve this problem, a pure mathematic method is proposed in this paper. By using the method, the central point potential (voltage) of the Y-type three phase windings can be worked out, so that the port voltages of three phase windings can be obtained and the model can be directly applied to BLDC motors. The theoretical procedure is given in detail.

The improved phase variable model has been implemented in the Simulink environment and used to analyze the performance of a high-speed surface mounted PM BLDC motor for driving embroidery machines [4]. In the model, key motor parameters such as winding flux, back *emf*, inductance and cogging torque are accurately determined based on magnetic field FEAs, which can take into account the details of motor structure and dimensions and the nonlinear properties of ferromagnetic cores. The simulations agree with the experimental results on the motor prototype operated with the BLDC control scheme.

## 2. Equation-based Phase Variable Model

The equation-based phase variable model of BLDC motor is given as

$$V_{abc} = r_{abc} i_{abc} + \frac{d\psi_{abc}}{dt} + e_{abc} \quad (1)$$

$$\psi_{abc} = L_{abc} i_{abc} \quad (2)$$

**Correspondence:** Youguang Guo, Faculty of Engineering, University of Technology, Sydney, PO Box 123, Broadway, NSW 2007, Australia,
email: youguang@eng.uts.edu.au.

$$T_m = \frac{e_a i_a + e_b i_b + e_c i_c}{\omega_r} + T_{cog} \tag{3}$$

$$J\frac{d\omega_r}{dt} = T_m - B\omega_r - T_L \tag{4}$$

$$\begin{bmatrix} \frac{d\psi_{sa}}{dt} \\ \frac{d\psi_{sb}}{dt} \\ \frac{d\psi_{sc}}{dt} \end{bmatrix} = \begin{bmatrix} \frac{\partial\psi_{sa}}{\partial i_a} & \frac{\partial\psi_{sa}}{\partial i_b} & \frac{\partial\psi_{sa}}{\partial i_c} \\ \frac{\partial\psi_{sb}}{\partial i_b} & \frac{\partial\psi_{sb}}{\partial i_b} & \frac{\partial\psi_{sb}}{\partial i_a} \\ \frac{\partial\psi_{sc}}{\partial i_a} & \frac{\partial\psi_{sc}}{\partial i_b} & \frac{\partial\psi_{sc}}{\partial i_c} \end{bmatrix} \begin{bmatrix} \frac{di_a}{dt} \\ \frac{di_b}{dt} \\ \frac{di_c}{dt} \end{bmatrix} + \begin{bmatrix} \frac{\partial\psi_{sa}}{\partial\theta} \\ \frac{\partial\psi_{sb}}{\partial\theta} \\ \frac{\partial\psi_{sc}}{\partial\theta} \end{bmatrix} \frac{d\theta}{dt}$$

$$= \begin{bmatrix} L_{aa} & L_{ab} & L_{ac} \\ L_{ba} & L_{bb} & L_{bc} \\ L_{ca} & L_{cb} & L_{cc} \end{bmatrix} \begin{bmatrix} \frac{di_a}{dt} \\ \frac{di_b}{dt} \\ \frac{di_c}{dt} \end{bmatrix} + \begin{bmatrix} \frac{dL_{aa}}{d\theta} & \frac{dL_{ab}}{d\theta} & \frac{dL_{ac}}{d\theta} \\ \frac{dL_{ba}}{d\theta} & \frac{dL_{bb}}{d\theta} & \frac{dL_{bc}}{d\theta} \\ \frac{dL_{ca}}{d\theta} & \frac{dL_{cb}}{d\theta} & \frac{dL_{cc}}{d\theta} \end{bmatrix} \begin{bmatrix} i_a \\ i_b \\ i_c \end{bmatrix} p\omega_r \tag{5}$$

$$\begin{bmatrix} v_a \\ v_b \\ v_c \end{bmatrix} = \begin{bmatrix} r_a & 0 & 0 \\ 0 & r_b & 0 \\ 0 & 0 & r_c \end{bmatrix} \begin{bmatrix} i_a \\ i_b \\ i_c \end{bmatrix} + \begin{bmatrix} L_{aa} & L_{ab} & L_{ac} \\ L_{ba} & L_{bb} & L_{bc} \\ L_{ca} & L_{cb} & L_{cc} \end{bmatrix} \begin{bmatrix} \frac{di_a}{dt} \\ \frac{di_b}{dt} \\ \frac{di_c}{dt} \end{bmatrix}$$

$$+ \begin{bmatrix} \frac{dL_{aa}}{d\theta} & \frac{dL_{ab}}{d\theta} & \frac{dL_{ac}}{d\theta} \\ \frac{dL_{ba}}{d\theta} & \frac{dL_{bb}}{d\theta} & \frac{dL_{bc}}{d\theta} \\ \frac{dL_{ca}}{d\theta} & \frac{dL_{cb}}{d\theta} & \frac{dL_{cc}}{d\theta} \end{bmatrix} \begin{bmatrix} i_a \\ i_b \\ i_c \end{bmatrix} p\omega_r + \begin{bmatrix} e_a \\ e_b \\ e_c \end{bmatrix} \tag{6}$$

$$L_{ab} = L_{ba},\ L_{bc} = L_{cb},\ L_{ca} = L_{ac} \tag{7}$$

$$r_a = r_b = r_c \tag{8}$$

$$i_a + i_b + i_c = 0 \tag{9}$$

where $L_{abc}$ is the inductance matrix and the difference between apparent and differential inductances is ignored here, $\psi_{sj}$ ($j$=$a$,$b$,$c$) is the flux linkage of phase winding $j$, and $p$ is the number of pole-pairs. The rest of parameters are used as their conventional meanings. The profiles of $L_{abc}$, $e_{abc}$ and $T_{cog}$ are obtained from the nonlinear transient FE solutions, in which the rotor position dependence and the saturation effect are considered. The stator windings are three-phase symmetrical.

## 3. Calculation of the Central Point Voltage

Suppose the electrical potentials (voltages) of terminals $a$, $b$, $c$ and $N$ (the central point) are $U_a$, $U_b$, $U_c$ and $U_N$, respectively, one can obtain

$$\begin{bmatrix} v_a \\ v_b \\ v_c \end{bmatrix} = \begin{bmatrix} U_a - U_N \\ U_b - U_N \\ U_c - U_N \end{bmatrix} \tag{10}$$

Then

$$U_N = \frac{\sum_{j=a}^{c}(U_j - v_j)}{3} \tag{11}$$

Substituting (6) into (11) and considering (9), the central point voltage is expressed as

$$U_N = \frac{[U_a - (L_{aa} + L_{ba} + L_{ca})\frac{di_a}{dt} - \frac{d(L_{aa} + L_{ba} + L_{ca})}{d\theta} i_a\omega]}{3}$$
$$+ \frac{[U_b - (L_{ab} + L_{bb} + L_{cb})\frac{di_b}{dt} - \frac{d(L_{ab} + L_{bb} + L_{cb})}{d\theta} i_b\omega]}{3}$$
$$+ \frac{[U_c - (L_{ac} + L_{bc} + L_{cc})\frac{di_c}{dt} - \frac{d(L_{ac} + L_{bc} + L_{cc})}{d\theta} i_c\omega]}{3}$$
$$- \frac{[e_a(\theta) + e_b(\theta) + e_c(\theta)]}{3} \tag{12}$$

The values of $U_a$, $U_b$ and $U_c$ are determined by the switching state of inverter with three phases, the state of PWM and the phase currents. When one phase current, e.g. $i_a$ of phase $a$, is zero, and the associated circuit is open-circuited (i.e. the winding of phase $a$ is in a non-energized condition), under the consideration of (7)-(9), $U_N$ and $U_a$ can be obtained by

$$U_N = \frac{[U_b - L_{bb}\frac{di_b}{dt} - \frac{dL_{bb}}{d\theta} i_b\omega]}{2}$$
$$+ \frac{[U_c - L_{cc}\frac{di_c}{dt} - \frac{dL_{cc}}{d\theta} i_c\omega]}{2} - \frac{[e_b(\theta) + e_c(\theta)]}{2} \tag{13}$$

$$U_a = U_N + (L_{aa} + L_{ba} + L_{ca})\frac{di_a}{dt} + e_a(\theta)$$
$$+ (\frac{dL_{ab}}{d\theta} i_b + \frac{dL_{ac}}{d\theta} i_c)\omega + (L_{ab}\frac{di_b}{dt} + L_{ac}\frac{di_c}{dt}) \tag{14}$$

When the winding current is not equal to zero and PWM is under the state of duty-off, the voltage of input port of phase *a* can be decided by

$$\text{if } i_a>0, \text{ then } U_a=U_{bus} \tag{15}$$

$$\text{if } i_a<0, \text{ then } U_a=0 \tag{16}$$

where $U_{bus}$ is the voltage of input power line. According to (13)-(16), one can work out the input port voltages of three phases and their central point, and hence the three phase voltages $v_a$, $v_b$ and $v_c$.

Referring to (6), the voltage equation of phase *a* is

$$v_a = (r_a i_a + L_{aa}\frac{di_a}{dt}) + (L_{ab}\frac{di_b}{dt} + L_{ac}\frac{di_c}{dt}) + (\frac{dL_{aa}}{d\theta}i_a + \frac{dL_{ab}}{d\theta}i_b + \frac{dL_{ac}}{d\theta}i_c)\omega + e_a \tag{17}$$

By defining that

$$v_{am} = (L_{ab}\frac{di_b}{dt} + L_{ac}\frac{di_c}{dt}) + (\frac{dL_{aa}}{d\theta}i_a + \frac{dL_{ab}}{d\theta}i_b + \frac{dL_{ac}}{d\theta}i_c)\omega \tag{18}$$

we have

$$v_a = (r_a i_a + L_{aa}\frac{di_a}{dt}) + v_{am} + e_a \tag{19}$$

$$v_a' = v_a - v_{am} = (r_a i_a + L_{aa}\frac{di_a}{dt}) + e_a \tag{20}$$

Similarly,

$$v_{bm} = (L_{ba}\frac{di_a}{dt} + L_{bc}\frac{di_c}{dt}) + (\frac{dL_{ba}}{d\theta}i_a + \frac{dL_{bb}}{d\theta}i_b + \frac{dL_{bc}}{d\theta}i_c)\omega \tag{21}$$

$$v_b = (r_b i_b + L_{bb}\frac{di_b}{dt}) + v_{bm} + e_b \tag{22}$$

$$v_b' = v_b - v_{bm} = (r_b i_b + L_{bb}\frac{di_b}{dt}) + e_b \tag{23}$$

$$v_{cm} = (L_{ca}\frac{di_a}{dt} + L_{cb}\frac{di_b}{dt}) + (\frac{dL_{ca}}{d\theta}i_a + \frac{dL_{cb}}{d\theta}i_b + \frac{dL_{cc}}{d\theta}i_c)\omega_r \tag{24}$$

$$v_c = (r_c i_c + L_{cc}\frac{di_c}{dt}) + v_{cm} + e_c \tag{25}$$

$$v_c' = v_c - v_{cm} = (r_c i_c + L_{cc}\frac{di_c}{dt}) + e_c \tag{26}$$

## 4. Performance Simulation of BLDC Motor

### *4.1 Simulink-based phase variable model*

According to (1)-(16), a complete Matlab/Simulink-based phase variable model is built as shown in Fig. 1, where $v_{am}$, $v_{bm}$ and $v_{cm}$, $v_a$, $v_b$ and $v_c$, $v'_a$, $v'_b$ and $v'_c$ can be obtained from Matlab functions based on (17)-(26). The rest of work is similar to the modeling of a conventional DC motor, so the proposed model can be easily realized in the Simulink environment.

### *4.2 Performance Evaluation*

As an example, the presented improved phase variable model has been used to analyze a surface mounted PM BLDC motor, which has been developed for driving high-speed embroidery machines [4]. Major parameters and dimensions of the motor include 4 poles, 12 stator slots, 3 phase single-layer windings, and the stator core dimensions are 38 mm for the inner diameter, 76 mm for the outer diameter, and 38 mm for the axial length, respectively. The motor is designed to deliver an output torque of 1.0 Nm at a speed of not less than 5000 rpm. The calculations of winding flux, back *emf*, inductances and cogging torque are reported in [4].

By using the improved phase variable model, comprehensive performances of the BLDC motor can be simulated, such as the curves of speed, current and torque during the start-up or transients when the load or power supply changes. For example, Fig. 2 illustrates the speed curve during the start-up with the full load of 1.0 Nm and the rated inverter voltage of 310 VDC. It can be seen that the motor speed can smoothly increase to the rated speed of 5000 rpm. Fig. 3 shows the bus current waveform.

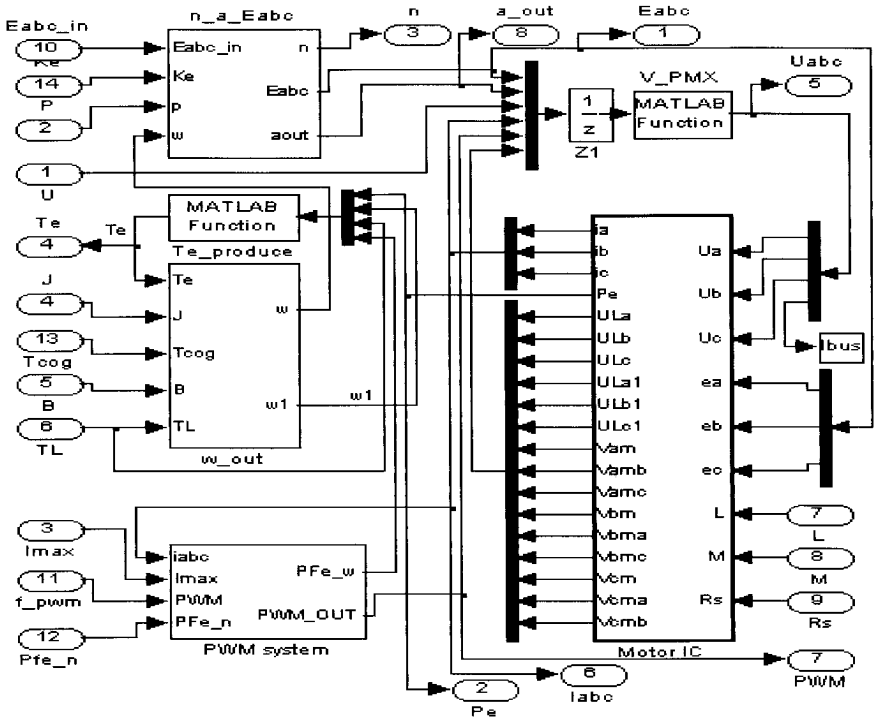


Fig. 1. Simulink-based improved phase variable model of BLDC motors

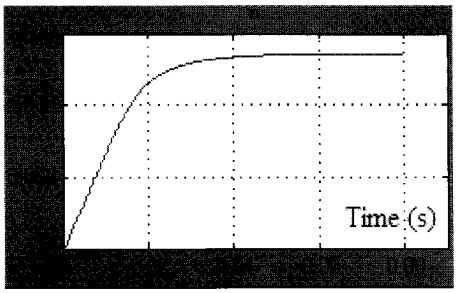


Fig. 2. Speed curve during start-up

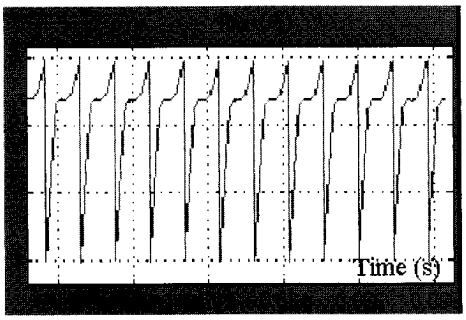


Fig. 3. Bus current waveform

## 5. Conclusion

This paper presents an improved phase variable model to evaluate the comprehensive performance of a PM brushless DC motor in both dynamic and steady conditions. A pure mathematical method is proposed to achieve the central point voltage of the Y-connected three phase windings so that the phase voltages can be obtained and the model can be directly applied to analyze the BLDC motor. The simulations on a high speed BLDC motor prototype show the validity of the model.

## References

[1] T. Kenjo, *Permanent Magnet and Brushless DC Motors*, Oxford University Press, 1985.

[2] O. A. Mohammed, S. Liu and Z. Liu, "A phase variable model of brushless DC motors based on finite element analysis and its coupling with external circuits," *IEEE Tran. Magn.*, Vol. 41, No. 5, pp. 1576-1579, 2005.

[3] O. A. Mohammed, S. Liu and Z. Liu, "Physical modeling of PM sunchronous motors for integrated coupling with machine drives," *IEEE Tran. Magn.*, Vol. 41, No. 5, pp. 1628-1631, 2005.

[4] J. X. Chen, Y. G. Guo and J. G. Zhu, "Comprehensive performance evaluation of brushless DC motors using an improved phase variable Model," *Asia-Pacific Symposium on Applied Electromagnetics*, Sydney, Australia, 2006, Full paper accepted for publication in the *Journal of Japanese Society of Applied Electromagnetics and Mechanics*.

Received: 20 July 2006/Revised: 31 January 2007